The Role of Terminal Group Position in Triphenylamine Based Self-Assembled Hole-Selective Molecules in Perovskite Solar Cells

Ece Aktas,[1,2] Rajesh Pudi,[1] Nga Phung,[3,#] Robert Wenisch,[4] Luca Gregori, [5,6] Daniele Meggiolaro,[5] Marion A. Flatken,[3] Filippo De Angelis,[6,7] Iver Lauermann,[4] Antonio Abate,[3,8*] and Emilio Palomares,[1,9*]

[1]Institute of Chemical Research of Catalonia (ICIQ-BIST). Avda. Països Catalans, 16. Tarragona. E-43007. Spain.

[2]Departament de Química-Física i Inorgànica. URV. E-43007. Spain.

[3]Helmholtz-Zentrum Berlin für Materialien und Energie GmbH, Hahn-Meitner-Platz 1, 14109 Berlin, Germany.

[4]PVcomB/Helmholtz-Zentrum Berlin für Materialien und Energie, Schwarzschildstraße 3,12489 Berlin, Germany.

[5]Computational Laboratory for Hybrid/Organic Photovoltaics (CLHYO), Istituto CNR di Scienze e Tecnologie Chimiche ''Giulio Natta'' (CNR-SCITEC), Via Elce di Sotto 8, 06123 Perugia, Italy.

[6]Department of Chemistry, Biology and Biotechnology, University of Perugia, Via Elce di Sotto 8, 06123 Perugia, Italy.

[7]Department of Natural Sciences & Mathematics, College of Sciences & Human Studies, Prince Mohammad Bin Fahd University, Saudi Arabia.

[8]Department of Chemical, Materials and Production Engineering, University of Naples Federico II, Piazzale Tecchio 80, 80125 Fuorigrotta, Italy.

[9]ICREA. Passeig LLuís Companys 23. E-08010. Spain.

[#]Present address: Department of Applied Physics, Eindhoven University of Technology, 5600 MB Eindhoven, the Netherlands.

Email of corresponding authors:

antonio.abate@helmholtz-berlin.de

antonio.abate@unina.it

epalomares@ICIQ.es

Abstract

The application of self-assembled molecules (SAMs) as a charge selective layer in perovskite solar cells has gained tremendous attention. As a result, highly efficient and stable devices have been released with stand-alone SAMs binding ITO substrates. However, further structural understanding of the effect of SAM in perovskite solar cells (PSCs) is required. Herein, three triphenylamine-based molecules with differently positioned methoxy substituents have been synthesised that can self-assemble onto the metal oxide layers that selectively extract holes. They have been effectively employed in p-i-n PSCs with a power conversion efficiency of up to 20%. We found that the perovskite deposited onto SAMs made by *para-&ortho-* substituted hole selective contacts provides large grain thin film formation increasing the power conversion efficiencies. Density functional theory predicts that *para-&ortho-* substituted position SAM might be formed a well-ordered structure by improving the SAM's arrangement and in consequence, enhancing its stability on the metal oxide surface. We believe this result will benchmark for the design of further SAMs.

Introduction

The perovskite solar cell (PSC) is one kind of renewable photovoltaic energy source that attracts attention owing to outstanding optoelectronic properties like low exciton binding energy,[1] high absorption coefficient,[2] long charge carrier lifetime and diffusion length,[3] and tuneable bandgap.[4] The power conversion efficiency (PCE) of the PSCs has dramatically improved from 3.8% to above 25% within a decade.[5,6] PSCs are made of a light-absorbing perovskite layer sandwiched between the charge selective layers. These selective layers play a key role in extracting holes and electrons from perovskite films and transporting these charges to be collected at the electrodes.[7]

The charge selective layers significantly impact the PSCs' final power conversion efficiency and stability.[8,9] Over the last two decades, the major research in charge selective materials has been focused on designing and synthesising new hole selective materials for improving the power conversion efficiency and stability of photovoltaic devices by replacing high-priced commercial ones.[10–12] Initially, hole selective layers (HSLs) provide the basis for a homogeneous film morphology and directly affect the crystal properties of the perovskite absorber layer in p-i-n configuration PSCs. A Poly[bis(4-phenyl)(2,4,6-trimethylphenyl)amine (PTAA) layer is widely used as an HSL in p-i-n configuration PSCs, its highly hydrophobic properties lead to increased perovskite grain sizes and directly affects the performance of the perovskite devices.[13] On the other hand, its highly hydrophobic properties will reduce the repeatability of the perovskite devices and causes pinholes after depositing the perovskite layer.[14,15] Self-assembled molecules (SAMs) have recently been used in p-i-n PSCs as HSLs, owing to advantages being cost-effectiveness, stability, and absence of additives.[16–18] Additionally, SAMs provide large-scale deposition capability due to their capacity to use different types of deposition techniques. SAMs typically consist of three groups; an anchoring group that connects the small molecules to the metal oxide surface via chemical bonding, a spacer that controls the packing geometry, and a terminal group that adjusts the surface and interface properties.[19–21] The control of interface properties has drawn attention due to improving the charge extraction with better energy alignment and reduced trap density.[22,23] Moreover, the terminal group determines the wettability of

the SAMs, which affects the grain size and consequently the grain boundaries of the perovskite layer.[13] Furthermore, the presence of methoxy groups in SAMs creates wetting surfaces that ensure excellent covering and reproducibility of the perovskite layer.[24]

The main purpose of our previous study was to investigate the affect of the spacer moiety of SAMs on the thermal stability of the PSCs. We demonstrated that the PTAA layer based devices exhibited inferior stability compared to SAMs.[25] In this study, triphenylamine (TPA) moiety is selected as a spacer, which is drawn attention due to their good thermal and morphological stabile properties in PSCs.[26] The glass transition temperatures (T_g) of HSLs are higher than the operating temperature (~100 °C), the molecular motion is minimised, therefore, transition to the crystalline state is reduced. In the opposite case, it leads to the intensified formation of grain boundaries, which might trap charge carriers and eventually result in degradation of device performance.[27] Besides, TPA exhibits a good electron donor property with two key features: easy oxidizability of the amine nitrogen atom and the ability to carry positive charge efficiently.[28] Having high T_g and low ionization potentials are important for HSL-based extremely stable and efficient PSCs.[29,30]

Herein, we investigate how the methoxy (-OMe) group positions in TPA-based SAMs affect the electronic properties, the perovskite solar cell performance, and stability. According to the literature, the -OMe group might has electron-donating and electron-withdrawing behaviours under resonance stabilisation or due to its inductive effect, respectively.[31] Hammett demonstrated the substitution position can introduce electron-donating or electron-withdrawing properties in the *para*- and *meta*-positions, respectively, while the *ortho*-position causes more a steric hindrance.[32] Furthermore, Seok and co-workers revealed that the different arrangements of the -OMe groups affect the energy of the highest occupied molecular orbital (HOMO) and the lowest unoccupied molecular orbital (LUMO). The higher LUMO energy level of small molecule as an electron blocking layer enhanced fill factor (FF) value.[31]

In this work, the -OMe substituents are positioned in TPA-based small molecule structure on *para-&ortho*- (RC24), *ortho-&meta*- (RC25), and *para-&meta*- (RC34) and their structure-activity relationships as the HSL are explored in PSCs. We aim

to prove which substitution positions could give a suitable energy level to ensure high PSCs performance, likewise changing the wettability of the HSLs and increasing the grain size of perovskite. Furthermore, density functional theory (DFT) calculations completed our results by proving how the substitution position can affect having an ordered and stable layer on the metal oxide surface. The three SAMs have provided reproducible triple cation perovskite devices with the highest PCE reaching over 19.5% at one sun AM 1.5 G illumination. This study demonstrates that the -OMe groups' position affects of minor importance to the PSCs performance and quasi-steady-state efficiency. On average, the *para-&ortho-* position SAM has slightly higher PCE compared to other positions.

Results and Discussion

Figure 1 a shows the synthesis pathway of the new TPA-based SAMs, where *4-(bis(2',4'-dimethoxy-[1,1'-biphenyl]-4-yl)amino)benzoic acid* **(RC24)**, *4-(bis(2',5'-dimethoxy-[1,1'-biphenyl]-4-yl)amino)benzoic acid* **(RC25)** and *4-(bis(3',4'-dimethoxy-[1,1'-biphenyl]-4-yl)amino)benzoic acid* **(RC34)** have a TPA moiety as an electron donor unit. TPA based self-assembled moieties are modified with methoxy substituents due to assisting in lowering the oxidation potential and increasing the solubility of the molecules.[26] The methoxy substituents are placed in *para-&ortho-*, *ortho-&meta-*, and *para-&meta-* positions as a terminal group. The methoxy substituent position's alignment mainly affects the work function, photophysical and surface properties of the molecule, which are crucially important for the perovskite device performance. The carboxylic acid is preferred as an anchorage to increase the coverage ratio of SAMs along the ITO surface and stabilises this surface by attaching chemically to the -OH group.[16] The synthetic details of the TPA-based SAMs are presented in the SI.

Initially, we have demonstrated that the TPA-based SAMs are chemically attached to the -OH group of the indium-tin-oxide (ITO) by using X-ray photoelectron spectroscopy (XPS). The chemical reaction between the anchor group (carboxylic acid, phosphoric acid, etc.) and the surface group (-OH) of the metal oxide can be defined as a condensation reaction that produces ester-type linkages (O-C=O).[33–35] The C1s spectra of the surface are decomposed into four peaks assigned to C-H

and C-C bonds at 284.7 eV, 284.8 eV, and 284.5 eV, to C-O bonds at 285.7 eV, 285.8 eV, and 285.6 eV, to HO-C=O attributed bonds at 286.7 eV, 286.8 eV and 286.6 eV, and to O-C=O bonds at 288.9 eV, 289.1 eV and 289.0 eV for RC24, RC25 and RC34, respectively (Figure 1b).[36,37] The O1s spectra decomposed into four peaks are dedicated to the In-O bond at 530.0 eV, to surface hydroxides at 530.9 eV, to the C-O bond at 531.8 eV for all SAMs, and to the C=O bond at 533.1 eV for RC24 and 533.0 eV for RC25 and RC34 (Figure 1c).[38] The bare ITO surface exhibits common O1s and C1s peaks compared to the SAM-deposited ITO surface, which is shown in Figures S1a and S1b that can be caused by solvent residues from the cleaning procedure as observed in the previous study. The description of the XPS method and the summarised fitting data of the C1s and O1s spectrum are given in the supporting information (see Table S1, ESI†).

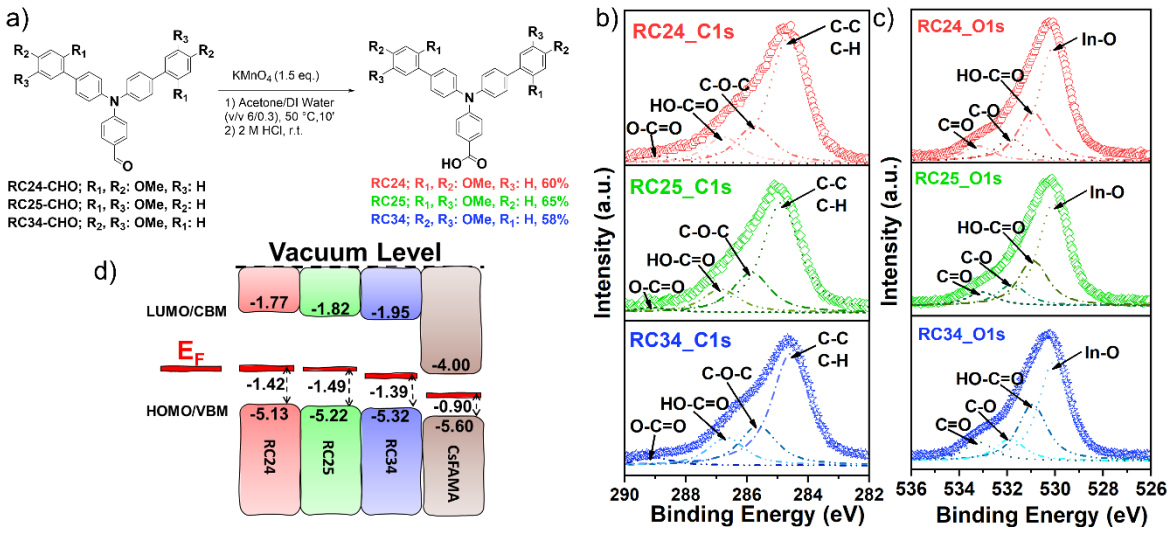

Figure 1. *a) The syntheses pathway of RC24, RC25, and RC34. b) XPS high-resolution survey spectra of b) C1s and c) O1s for RC24, RC25, and RC34. d) Energy alignment of different layers. The band edge positions of RC24, RC25, RC34 and CsFAMA layers from UPS measurements in a schematic representation.*

After assigning the chemical bonds of the SAMs on the ITO surface, we investigated the corresponding energetic properties to demonstrate their hole selective abilities for PSCs. Herein, we have chosen the $Cs_{0.05}FA_{0.79}MA_{0.16}Pb(I_{0.84}Br_{0.16})_3$ (onwards labelled as CsFAMA) perovskite as an absorber layer, owing to have higher device performance and stability, inducing highly uniform perovskite grains and increasing device reproducibility.[39] TPA-based SAM's LUMO energy levels are calculated by

utilising the optical bandgap, which is estimated from the absorption edge wavelength ($\lambda_{a.e.}$) using UV-Vis measurements (see Figure S2 and Table S2, ESI†). The optical bandgap energies are assumed equal to electronic bandgap of the SAMs and these values are added to the HOMO energy levels to determine LUMO energy levels (for details see the method section, ESI†).[31,40] The valence band (VBM) and the Fermi level (E_F) values of RC24, RC25, RC34, and CsFAMA perovskite are determined by ultra-violet photoelectron spectroscopy (UPS) (see Figure S3, ESI†) and schematically displayed in Figure 1d where all values refer to the vacuum level.[41] The RC24 with *para-& ortho-* positioned -OMe substituents exhibit slightly lower oxidation potential as a result of resonance effect of substituent position and it has better electron blocking character than RC25 and RC34, owing to higher LUMO energy level.[42] Furthermore, the solution-based SAM molecules' stability test is carried out by cyclic voltammetry measurements (Figure S4, ESI†). These tests showed SAM molecules have a stable reduction state after applied highly oxidation potential.[43]

To understand the different role of different positioned terminal groups on top of the ITO surface, we focused on the surface's wettability after the deposition of SAMs. We used contact angle measurements to determine the SAMs covered ITO surface wettability, performed with water (for details see the method section, ESI†). The -OMe group's position influences the hydrophobicity of SAMs in the following order: RC34 < RC25 < RC24. The contact angle as a measure of wettability is 42.0° for the *para-&ortho-* positioning, for the *ortho-&meta-* positioning 38.3° and 32.3° for the *para-&meta-* positioning (Figure 2a). The different position of the methoxy substituents in TPA-based SAMs shows a strong influence on the morphology of the obtained perovskite films (Figure 3), as discussed later.

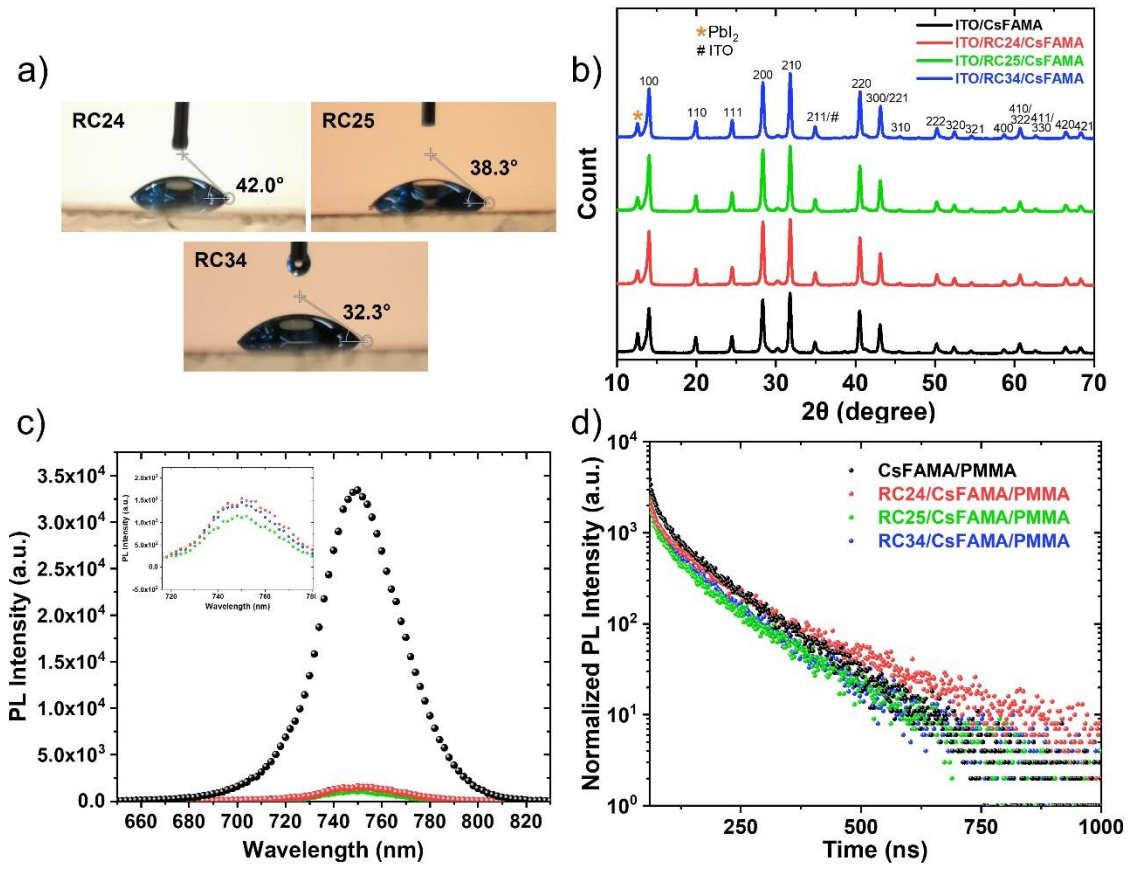

Figure 2. *a) Contact angle measurements on the RC24, RC25, and RC34 surfaces. b) X-ray diffraction patterns of perovskite layers grown on bare ITO, ITO/RC24, ITO/RC25, and ITO/RC34. The patterns are well in agreement with literature containing similar perovskite compounds. c) Luminescence emission band upon excitation at λ_{ex}=470 nm for the CsFAMA/PMMA, RC24/CsFAMA/PMMA, RC25/CsFAMA/PMMA and RC34/CsFAMA/PMMA (total thickness of 550-600 nm) at room temperature. d) Luminescence emission decays (λ_{ex}=470 nm) measured for 1000 ns for CsFAMA/PMMA, RC24/CsFAMA/PMMA, RC25/CsFAMA/PMMA and RC34/CsFAMA/PMMA on ITO coated glass substrate at room temperature.*

Figure 2c shows the photoluminescence spectrum of the CsFAMA film in a variety of bilayer configurations, including ITO/CsFAMA, ITO/RC24/CsFAMA, ITO/RC25/CsFAMA, and ITO/RC34/CsFAMA. The photoluminescence peak at 750 nm entirely agrees with previous reports of emission from CsFAMA[39], and the spectral position of the emission is stable among all the samples. Emission from the CsFAMA perovskite is almost entirely quenched upon contact with SAMs. RC34 based perovskite film has slightly lower, yet noticeably, photoluminescence yield than RC24 and RC34 as shown in enlarged PL image in Figure 2c, that shows their efficient hole transporting character. Additionally, we used time-resolved photoluminescence (TRPL) to investigate the radiative decay dynamics using λ_{ex}= 470 nm as excitation wavelength as shown in Figure 2d, which is acquired with a

time-correlated single-photon counting (TCSPC) technique. Here, two different decay profiles for RC24 and one decay profile for RC25 and RC34 are observed, fitted to a bi-exponential function, $y=A_1\ exp(-t/\tau_1)+A_2\ exp(-t/\tau_2)$[25] as in the earlier study.[44] We assign the slower decay (τ_2) to the bimolecular recombination, while the fast decay (τ_1) corresponds to trap filling for SAM-based perovskite films.[45] The calculated lifetimes τ_1 are 21 ns, 20 ns, 17 ns, and 19 ns for the CsFAMA perovskite, RC24, RC25, and RC34 respectively, while the lifetimes τ_2 of the CsFAMA perovskite, RC24, RC25, and RC34 are 122 ns, 130 ns, 115 ns, and 107 ns respectively (see Table S3, ESI†). Our hypothesis is that the lifetime τ_2 is due to either the passivation of defects at the interface between the SAMs and the perovkskite or it may well be to the different crystallinity of the perovskite after the initial nucleation of the fist nanometers of the film in direct contact with the SAMs. For instance, the RC24 will have different effects[46] as seen by the increased PL yield, compared to RC25 and RC34. It has been reported that the presence of the Lewis acid-base interactions[47] between the amino group in TPA and the positively charged defects such as under-coordinated Pb^{2+} in the perovskite cause passivation of surface defects and significantly decreases the non-radiative recombination in perovskite films.[48–50] This was our initial motivation for the synthesis of the molecules used in this work. Moreover, TPA-based SAMs exhibit good thermal and morphological stability during device fabrication and general operating conditions.

The thermal behaviour of RC24, RC25, and RC34 is analysed by differential scanning calorimetry (DSC) and thermogravimetry analysis (TGA) (see Table S4, Figure S5, ESI†). TGA showed remarkably high thermal stability with decomposition temperatures (5% weight loss) that are 347 °C, 383 °C, and 386 °C for RC24, RC25, and RC34, respectively. Likewise, DSC confirmed elevated T_g during the second heating cycle for RC24, RC25, and RC34 which are 190 °C, 196 °C, and 197 °C, respectively. The fact that TPA-based SAMs exist in both amorphous and semi-crystalline states explains their uniform coating when annealing the perovskite films at 100 °C.[51]

To examine the effect of the substitution position on perovskite films, the perovskite layers grown on SAMs are characterised by scanning electron microscopy (SEM). Figure 3 shows the full cross-sectional device, the surface morphology, and grain

size distribution of the perovskite thin film grown on SAMs. The perovskite thin films are uniform, cover the entire substrates, and are free of pinholes. Therefore, the bright small grains can be assigned to PbI_2 due to an excess concentration in the perovskite thin film that can improve the device performance, as reported in previous studies.[52,53] The perovskite layer that is grown on RC24 with *para-&ortho-* positioned methoxy substituents shows larger crystal grains and fewer grain boundaries with an average grain size of about 385±106 nm compared to 357±185 nm for RC25 and 301±85 nm for RC34. However, we acknowledge that SEM images are inadequate to identify the perovskite grain size distribution.[54] To further characterise the crystallite size of the perovskite layer deposited on the different SAMs, we performed Le Bail analysis on the corresponding XRD patterns (fitted patterns can be found in Figure S6, ESI†).[55] The domain size of the perovskite can be quantified by the Lorentzian contribution to the peak broadening of the perovskite diffracted peaks in the XRD patterns. Le Bail analysis demonstrates that RC24-based perovskite exhibits the largest domain size (approximately 100 nm), whereas perovskite layers on RC25 and RC34 domain sizes of 77 nm and 70 nm, respectively, which agrees with the results given by SEM images. We note that a domain is the largest unit with the same orientation, and a grain can consist of multiple domains. Furthermore, the SEM cross-sectional images of RC25 and RC34 in Figure 3 indicate small grains at the interface of SAM/perovskite and grain boundaries in the vertical direction. In contrast, the perovskite layer grown on RC24 seems to have a monolithic grain structure. This can directly affect the charge transport and device's performance in a quasi-steady-state condition.

By combining the average grain size with the hydrophobicity discussed previously (RC34 < RC25 < RC24), it is becoming evident that these two parameters correlate. Bi and co-workers showed the non-wetting substrate provides a higher grain boundary mobility and allows the growth of larger grains by the surface tension dragging force.[13,56] Concisely, the position of a suitable substituent is critical to the formation of uniform perovskite films with large grain sizes, which directly affects the perovskite device performance. Additionally, the large grain size is vital for perovskite solar cells due to transporting/collecting charge carriers efficiently and reducing charge recombination.[13,57,58]

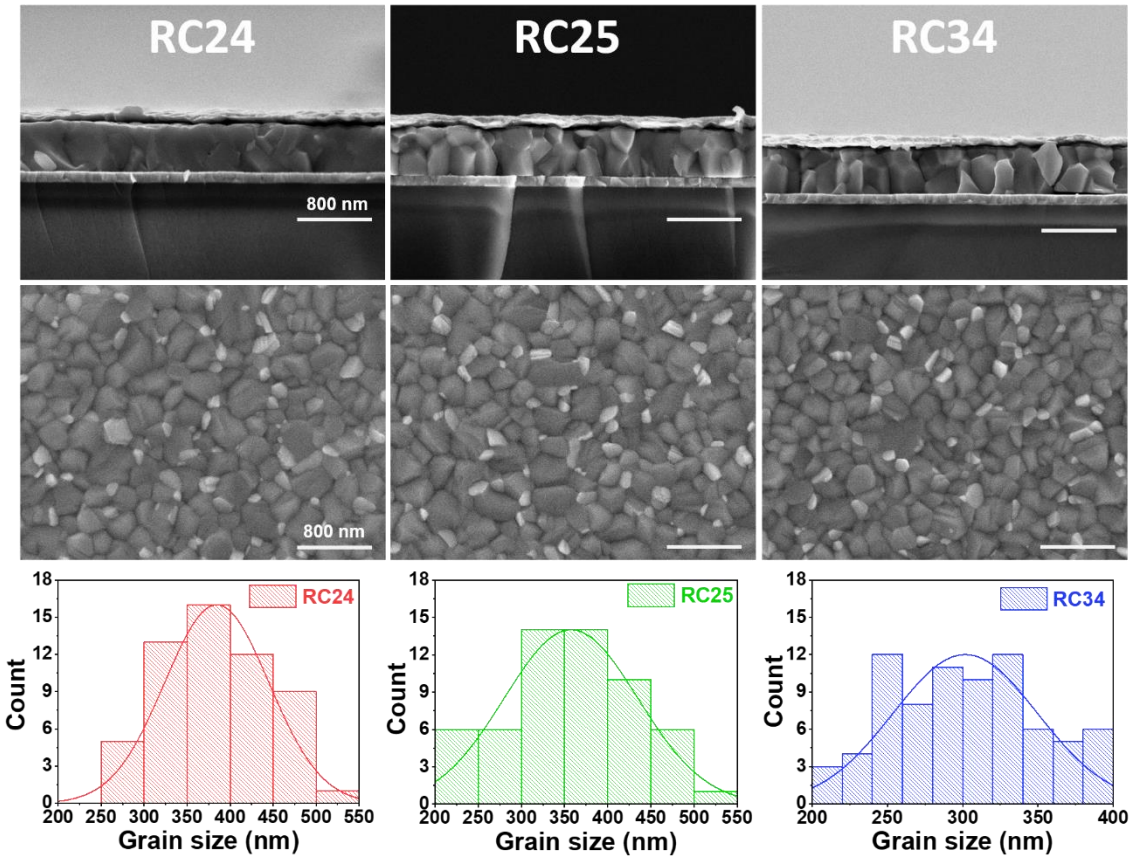

Figure 3. *Scanning electron microscopic images of the top view of perovskite layers grown on ITO/RC24, ITO/RC25, and ITO/RC34 and their cross-sectional full device image shown above the top view for each SAM. The grain size distribution of the perovskite thin films based on SAMs are shown below the top view for each SAM. All scale bars are 800 nm.*

We have further fabricated perovskite solar cells to investigate the influences of differently positioned methoxy substituents in SAMs on the power conversion efficiency and stability. The state-of-the-art device architecture with ITO/SAM/CsFAMA/C_{60}/BCP/Cu sandwich architecture is used in this study.[39] TPA-based SAMs are deposited on top of the UV-O_3 treated ITO substrates using the dip-coating deposition process. Then, the perovskite (CsFAMA) layer is placed on top of the SAMs using the one-step method.[59] Following perovskite layer deposition, C_{60} is thermally evaporated graciously as an electron selective layer to passivate the grain boundaries and surfaces of perovskite films.[60,61] Afterwards, a thin layer of bathocuproine (BCP) is evaporated on top of the electron selective layer as a buffer layer for eliminating charge accumulation at the C_{60}/BCP/Cu interfaces.[62] A 100 nm copper (Cu) electrode is evaporated to complete the device. The experimental section gives all the fabrication processes of the perovskite solar cells.

All SAMs are deposited on top of the ITO substrates using a dip-coating method which is the most applied method for having a well-organised interface under the perovskite absorber. The unbound molecules could be eliminated with the used solvent by rinsing or an ultrasonic cleaning bath. A dip-coating method was optimised by using non-halogenated solvents thanks to the anchor group of SAMs. In this study, the most common non-halogenated solvents are used for optimising the effect of SAM on the performance of the perovskite solar cells. The statistically better performance of the RC24 and RC34 based perovskite devices with Ethanol (EtOH) and RC25 based devices with isopropanol (IPA) are shown by having higher FF (see Figure S7, ESI†). The best photovoltaic parameters of the solvent optimisation for each SAMs are summed up in Table S5, where the FF values of the RC24 have a significantly narrower distribution comparing to RC25 and RC34.

The best device's current density versus voltage (J-V) plots recorded from RC24, RC25, and RC34 measured at a scan rate of 100 mV/s are demonstrated in Figure 4a. Specifically, the open-circuit voltage (V_{OC}) of the RC24 SAM-based device is approximately 17 mV larger than of RC25 and RC34 SAM-based devices, while the scan direction is from V_{OC} to J_{SC}. In addition, An and co-workers demonstrated that with increasing average grain size, the V_{OC} could be significantly enhanced by over 200 mV with a slight increase in FF.[63] The best-achieved PCE of RC24, RC25, and RC34 is 19.8%, 19.6%, and 19.7%, surpassing the commercially available HSLs from literature, especially while using a PTAA layer in the same device structure in our previous study (Table 1).[25,64]

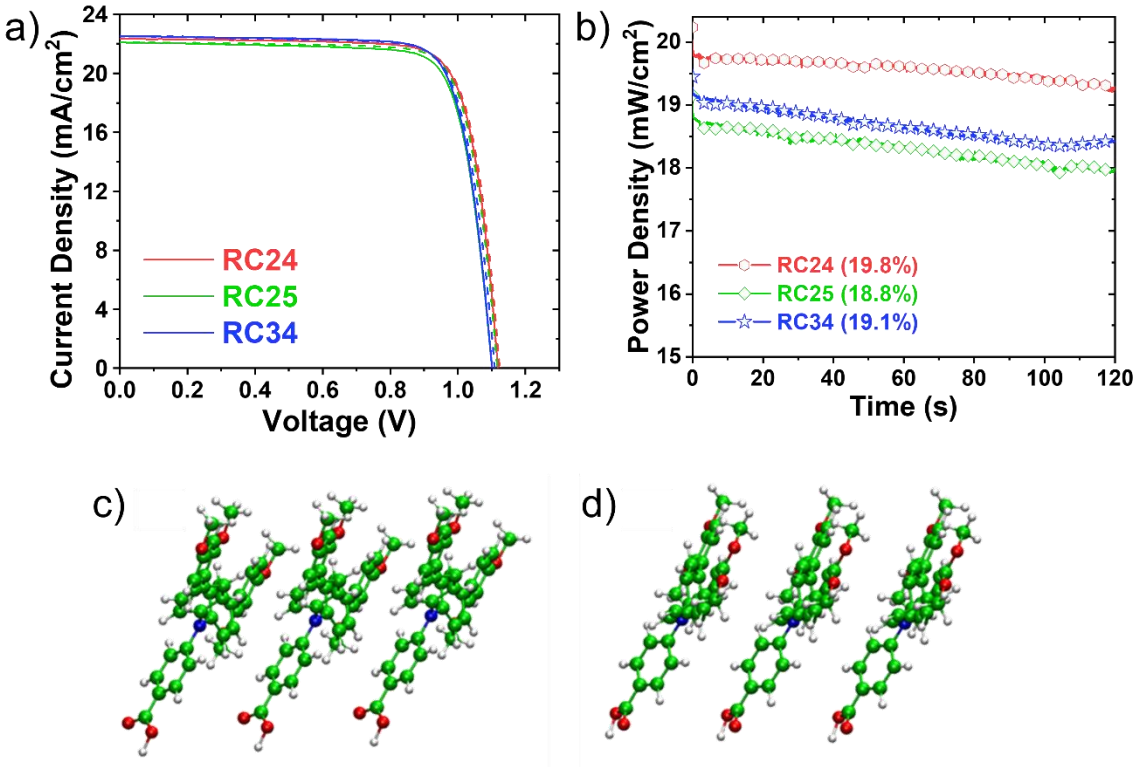

***Figure 4**. a) Best J-V curves from RC24, RC25 and RC34 in EtOH. b) Quasi-steady-state efficiency of best devices with RC24, RC25, and RC34. SAM for c) RC24 molecules d) RC34 molecules.*

The J-V scan of SAMs-HSL based full devices indicated a similar lower leakage current under dark conditions (see Figure S8b, ESI†). A low dark current is one of the proofs to show a high density of SAMs on the ITO surface. External quantum efficiency measurements (EQE) are done to understand how efficiently a perovskite layer transforms light into current.[65] The integrated $J_{SC,EQE}$ of the best devices is close to the $J_{SC,J-V}$ in Figure S8a, and the devices show an insignificant hysteresis index (HI) between reverse and forward J-V scans. The photovoltaic parameters of the best devices and the average grain size distribution is estimated as listed in Table 1.

***Table 1.** Photovoltaic parameters of the best performing devices based on different SAMs and PTAA with a scan speed of 100 mV/s and the average grain size distribution.*

SAMs	*Average Grain Size (nm)*	*$J_{SC,EQE}$ (mA/cm²)*	*$J_{SC,J-V}$ (mA/cm²)*	*V_{OC} (mV)*	*FF (%)*	*PCE (%)*	*HI (%)*
RC-24	385±106	21.5	22.3	1123	79	19.8	0.00
RC-25	357±185	21.4	22.1	1116	79	19.6	0.02

RC-34	301±85	21.3	22.5	1109	79	19.7	0.00
***PTAA**	-	21.2	21.9	1098	79	18.9	-0.01

*The given reference data has an identical device architecture and photovoltaic parameters are measured using exactly the same equipment.[25]

To understand the effect of a differently positioned methoxy substituent in SAMs with short-term perovskite device stability, maximum power point (MPP) tracks of the best devices are performed. After the first J-V scan, MPP tracks are made where RC25 and RC34 display a significantly lower performance over RC24. As can be seen in Figure 4b, RC24, RC25, and RC34 based perovskite cells lost around 3%, 4%, and 5% of their initial PCE after 120 seconds of MPP tracking, respectively. In addition, RC25 and RC34 devices exhibit a significant burn-in loss in the first few seconds at the MPP and continue to decrease afterwards. On the contrary, the *ortho-&para*-position substituted RC24 devices show a more stable MPP output. At first sight, this can be attributed to its high hydrophobicity (water contact angle 42.0°), which can influence the response of the devices as shown in literature.[66] More importantly, when the monolayer is created, the molecules link each other by the mean of dispersion interactions especially by π-π stacking between the phenyls group of nearby molecules, which tends to overlap. DFT calculations show that the monolayer formed by the RC24 molecule presents 0.12 eV larger interaction energy between pairs of molecules than RC34. This suggests that the RC24 molecules are more suited to form a more compact, ordered and thus stable monolayer, with respect to RC34, when adsorbed onto the ITO surface (Figure 4c and d). Moreover, previous reports show that mobile ions in the perovskite layers can be trapped at the grain boundaries, resulting in a longer transient in device response.[67,68] Thus, the lower grain boundary density in perovskite grown on RC24 leads to a slower decay slope, as can be seen in MPP tracking (Figure 4b).

Conclusion

In conclusion, we synthesised and characterised three new self-assembled hole selective molecules for application in p-i-n perovskite devices. TPA based-SAMs are demonstrated to be effective in enhancing the efficiency of perovskite devices to 19.8%. Our results provide a simple molecule design strategy for achieving reduced hysteresis and highly efficient perovskite devices. As we mentioned earlier, the -OMe group's existence increases the wettability of the metal oxide substrates, although

their position as a terminal group directly affects the device performance by increasing grain size. An enhanced crystal growth towards larger crystallite formation in the polycrystalline perovskite film reduces the grain boundaries density, which consequently reduces surface recombination, decreases hysteresis, and increases the PCE of the perovskite device. Lastly, DFT calculation showed that the terminal group of SAMs plays a critical role to form homogeneous and stable SAM on metal oxide surfaces apart from changing the surface and interface properties. This study provides new guidelines to understand the importance of the molecule design of the charge selective contact and their role in the efficiency and stability of the PSCs. Moreover, this study tends to provide a new perspective to the interfacial engineering of hole selective layer that might be also used in optoelectronic applications likewise light emitting diodes, etc.

Acknowledgments

EA, RP, and EP thank MINECO (projects CTQ2013-47183, CTQ2017-89814-P, and CTQ2017-85393-P) and SGR-AGAUR 2017SGR00978. EP is also thankful to ICIQ and ICREA for financial support. This result is part of a project that has received funding from the European Research Council (ERC) under the European Union's Horizon 2020 research and innovation programme grant agreement No. number 804519. IL and RW acknowledge financial support by the German Federal Ministry for Economic Affairs and Energy in the frame of the speedCIGS project (contract number 0334095E). EA thanks ICIQ for funding the internship in HZB. The authors thank Carola Klimm for taking SEM microscopic images.

Author contributions

EA, RP, and NP conceived the idea, formulated the project, and wrote the first draft of the manuscript under the supervision of EP and AA. RP synthesised RC24, RC25, and RC34. EA and MAF fabricated the devices and carried out the photophysical characterisation. NP carried out XRD measurement and structural analysis. EA carried out Time-Correlated Single Photon Counting Measurements. RW carried out X-ray Photoelectron Spectroscopy and Ultra-violet Photoelectron measurements

under the supervision of IL. LG and DM performed DFT calculations under the supervision of FDA. All authors participated in the discussion of the results and the manuscript writing, and finally, approved the submission.

Supporting Information

Synthesis details of SAMs, additional figures, including ^{1}H and ^{13}C NMR spectrums of newly synthesized molecules, UV-vis absorption spectra, PL spectra, Thermal analysis of molecules (TGA, DSC), statistic results of photovoltaic parameters, EQE, dark *J-V, XPS fitting data and energy level calculation details of SAMs with UPS, single scan cyclic voltammogram of SAMs with ferrocene, Le-Bail refinement from a laboratory XRD pattern of perovskite layer based on SAMs, DFT calculation details*

References

(1) Miyata, A.; Mitioglu, A.; Plochocka, P.; Portugall, O.; Wang, J. T.-W.; Stranks, S. D.; Snaith, H. J.; Nicholas, R. J. Direct Measurement of the Exciton Binding Energy and Effective Masses for Charge Carriers in Organic–Inorganic Tri-Halide Perovskites. *Nat. Phys.* **2015**, *11* (7), 582–587. https://doi.org/10.1038/nphys3357.

(2) Maes, J.; Balcaen, L.; Drijvers, E.; Zhao, Q.; De Roo, J.; Vantomme, A.; Vanhaecke, F.; Geiregat, P.; Hens, Z. Light Absorption Coefficient of CsPbBr3 Perovskite Nanocrystals. *J. Phys. Chem. Lett.* **2018**, *9* (11), 3093–3097. https://doi.org/10.1021/acs.jpclett.8b01065.

(3) Stranks, S. D.; Eperon, G. E.; Grancini, G.; Menelaou, C.; Alcocer, M. J. P.; Leijtens, T.; Herz, L. M.; Petrozza, A.; Snaith, H. J. Electron-Hole Diffusion Lengths Exceeding 1 Micrometer in an Organometal Trihalide Perovskite Absorber. *Science (80-.).* **2013**, *342* (6156), 341–344. https://doi.org/10.1126/science.1243982.

(4) Eperon, G. E.; Stranks, S. D.; Menelaou, C.; Johnston, M. B.; Herz, L. M.; Snaith, H. J. Formamidinium Lead Trihalide: A Broadly Tunable Perovskite for Efficient Planar Heterojunction Solar Cells. *Energy Environ. Sci.* **2014**, *7* (3), 982. https://doi.org/10.1039/c3ee43822h.

(5) Kojima, A.; Teshima, K.; Shirai, Y.; Miyasaka, T. Organometal Halide Perovskites as Visible-Light Sensitizers for Photovoltaic Cells. *J. Am. Chem. Soc.* **2009**, *131* (17), 6050–6051. https://doi.org/10.1021/ja809598r.

(6) NREL. Best Research-Cell Efficiency Chart https://www.nrel.gov/pv/cell-efficiency.html.

(7) Roose, B.; Wang, Q.; Abate, A. The Role of Charge Selective Contacts in Perovskite Solar Cell Stability. *Adv. Energy Mater.* **2019**, *9* (5), 1–20. https://doi.org/10.1002/aenm.201803140.

(8) Roose, B.; Wang, Q.; Abate, A. The Role of Charge Selective Contacts in Perovskite Solar Cell Stability. *Adv. Energy Mater.* **2018**, 1803140.

https://doi.org/10.1002/aenm.201803140.

(9) Shang, R.; Zhou, Z.; Nishioka, H.; Halim, H.; Furukawa, S.; Takei, I.; Ninomiya, N.; Nakamura, E. Disodium Benzodipyrrole Sulfonate as Neutral Hole-Transporting Materials for Perovskite Solar Cells. *J. Am. Chem. Soc.* **2018**, *140* (15), 5018–5022. https://doi.org/10.1021/jacs.8b01783.

(10) Yin, X.; Song, Z.; Li, Z.; Tang, W. Toward Ideal Hole Transport Materials: A Review on Recent Progress in Dopant-Free Hole Transport Materials for Fabricating Efficient and Stable Perovskite Solar Cells. *Energy Environ. Sci.* **2020**, *13* (11), 4057–4086. https://doi.org/10.1039/D0EE02337J.

(11) Liu, C.; Igci, C.; Yang, Y.; Syzgantseva, O. A.; Syzgantseva, M. A.; Rakstys, K.; Kanda, H.; Shibayama, N.; Ding, B.; Zhang, X.; Jankauskas, V.; Ding, Y.; Dai, S.; Dyson, P. J.; Nazeeruddin, M. K. Dopant-Free Hole Transport Materials Afford Efficient and Stable Inorganic Perovskite Solar Cells and Modules. *Angew. Chemie Int. Ed.* **2021**, *60* (37), 20489–20497. https://doi.org/10.1002/anie.202107774.

(12) Zhou, Z.; Qiang, Z.; Sakamaki, T.; Takei, I.; Shang, R.; Nakamura, E. Organic/Inorganic Hybrid p-Type Semiconductor Doping Affords Hole Transporting Layer Free Thin-Film Perovskite Solar Cells with High Stability. *ACS Appl. Mater. Interfaces* **2019**, *11* (25), 22603–22611. https://doi.org/10.1021/acsami.9b06513.

(13) Bi, C.; Wang, Q.; Shao, Y.; Yuan, Y.; Xiao, Z.; Huang, J. Non-Wetting Surface-Driven High-Aspect-Ratio Crystalline Grain Growth for Efficient Hybrid Perovskite Solar Cells. *Nat. Commun.* **2015**, *6*, 1–7. https://doi.org/10.1038/ncomms8747.

(14) Stolterfoht, M.; Wolff, C. M.; Amir, Y.; Paulke, A.; Perdigón-Toro, L.; Caprioglio, P.; Neher, D. Approaching the Fill Factor Shockley–Queisser Limit in Stable, Dopant-Free Triple Cation Perovskite Solar Cells. *Energy Environ. Sci.* **2017**, *10* (6), 1530–1539. https://doi.org/10.1039/C7EE00899F.

(15) Tzoganakis, N.; Feng, B.; Loizos, M.; Krassas, M.; Tsikritzis, D.; Zhuang, X.; Kymakis, E. Ultrathin PTAA Interlayer in Conjunction with Azulene Derivatives for the Fabrication of Inverted Perovskite Solar Cells. *J. Mater. Chem. C* **2021**, *9* (41), 14709–14719. https://doi.org/10.1039/d1tc02726c.

(16) Yalcin, E.; Can, M.; Rodriguez-Seco, C.; Aktas, E.; Pudi, R.; Cambarau, W.; Demic, S.; Palomares, E. Semiconductor Self-Assembled Monolayers as Selective Contacts for Efficient PiN Perovskite Solar Cells. *Energy Environ. Sci.* **2019**, *12* (1), 230–237. https://doi.org/10.1039/c8ee01831f.

(17) Magomedov, A.; Al-Ashouri, A.; Kasparavičius, E.; Strazdaite, S.; Niaura, G.; Jošt, M.; Malinauskas, T.; Albrecht, S.; Getautis, V. Self-Assembled Hole Transporting Monolayer for Highly Efficient Perovskite Solar Cells. *Adv. Energy Mater.* **2018**, *8* (32). https://doi.org/10.1002/aenm.201801892.

(18) Dai, Z.; Yadavalli, S. K.; Chen, M.; Abbaspourtamijani, A.; Qi, Y.; Padture, N. P. Interfacial Toughening with Self-Assembled Monolayers Enhances Perovskite Solar Cell Reliability. **2021**, *622* (May), 618–622.

(19) Canil, L.; Cramer, T.; Fraboni, B.; Ricciarelli, D.; Meggiolaro, D.; Singh, A.; Liu, M.; Rusu, M.; Wolff, C. M.; Phung, N.; Wang, Q.; Neher, D.; Unold, T.; Vivo, P.; Gagliardi, A.; De Angelis, F.; Abate, A. Tuning Halide Perovskite Energy Levels. *Energy Environ. Sci.* **2021**. https://doi.org/10.1039/d0ee02216k.

(20) Choi, K.; Choi, H.; Min, J.; Kim, T.; Kim, D.; Son, S. Y.; Kim, G. W.; Choi, J.; Park, T.

A Short Review on Interface Engineering of Perovskite Solar Cells: A Self-Assembled Monolayer and Its Roles. *Sol. RRL* **2020**, *4* (2), 1–20. https://doi.org/10.1002/solr.201900251.

(21) Wolff, C. M.; Canil, L.; Rehermann, C.; Ngoc Linh, N.; Zu, F.; Ralaiarisoa, M.; Caprioglio, P.; Fiedler, L.; Stolterfoht, M.; Kogikoski, S.; Bald, I.; Koch, N.; Unger, E. L.; Dittrich, T.; Abate, A.; Neher, D. Perfluorinated Self-Assembled Monolayers Enhance the Stability and Efficiency of Inverted Perovskite Solar Cells. *ACS Nano* **2020**, *14* (2), 1445–1456. https://doi.org/10.1021/acsnano.9b03268.

(22) Zuo, L.; Chen, Q.; De Marco, N.; Hsieh, Y. T.; Chen, H.; Sun, P.; Chang, S. Y.; Zhao, H.; Dong, S.; Yang, Y. Tailoring the Interfacial Chemical Interaction for High-Efficiency Perovskite Solar Cells. *Nano Lett.* **2017**, *17* (1), 269–275. https://doi.org/10.1021/acs.nanolett.6b04015.

(23) Cao, B.; He, X.; Fetterly, C. R.; Olsen, B. C.; Luber, E. J.; Buriak, J. M. Role of Interfacial Layers in Organic Solar Cells: Energy Level Pinning versus Phase Segregation. *ACS Appl. Mater. Interfaces* **2016**, acsami.6b02712. https://doi.org/10.1021/acsami.6b02712.

(24) Han, J.; Kwon, H.; Kim, E.; Kim, D. W.; Son, H. J.; Kim, D. H. Interfacial Engineering of a ZnO Electron Transporting Layer Using Self-Assembled Monolayers for High Performance and Stable Perovskite Solar Cells. *J. Mater. Chem. A* **2020**, *8* (4), 2105–2113. https://doi.org/10.1039/c9ta12750j.

(25) Aktas, E.; Phung, N.; Köbler, H.; González, D. A.; Méndez, M.; Kafedjiska, I.; Turren-Cruz, S.-H.; Wenisch, R.; Lauermann, I.; Abate, A.; Palomares, E. Understanding the Perovskite/Self-Assembled Selective Contact Interface for Ultra-Stable and Highly Efficient p–i–n Perovskite Solar Cells. *Energy Environ. Sci.* **2021**. https://doi.org/10.1039/D0EE03807E.

(26) Agarwala, P.; Kabra, D. A Review on Triphenylamine (TPA) Based Organic Hole Transport Materials (HTMs) for Dye Sensitized Solar Cells (DSSCs) and Perovskite Solar Cells (PSCs): Evolution and Molecular Engineering. *J. Mater. Chem. A* **2017**, *5* (4), 1348–1373. https://doi.org/10.1039/c6ta08449d.

(27) Shen, S.; Gao, L.; He, C.; Zhang, Z.; Sun, Q.; Li, Y. A Star-Shaped Oligothiophene with Triphenylamine as Core and Octyl Cyanoacetate as End Groups for Solution-Processed Organic Solar Cells. *Org. Electron. physics, Mater. Appl.* **2013**, *14* (3), 875–881. https://doi.org/10.1016/j.orgel.2012.12.030.

(28) Thelakkat, M. Star-Shaped, Dendrimeric and Polymeric Triarylamines as Photoconductors and Hole Transport Materials for Electro-Optical Applications. *Macromol. Mater. Eng.* **2002**, *287* (7), 442. https://doi.org/10.1002/1439-2054(20020701)287:7<442::AID-MAME442>3.0.CO;2-H.

(29) Jeon, N. J.; Na, H.; Jung, E. H.; Yang, T. Y.; Lee, Y. G.; Kim, G.; Shin, H. W.; Il Seok, S.; Lee, J.; Seo, J. A Fluorene-Terminated Hole-Transporting Material for Highly Efficient and Stable Perovskite Solar Cells. *Nat. Energy* **2018**, *3* (8), 682–689. https://doi.org/10.1038/s41560-018-0200-6.

(30) An, M. W.; Wu, B. S.; Wang, S.; Chen, Z. C.; Su, Y.; Deng, L. L.; Li, S. H.; Nan, Z. A.; Tian, H. R.; Liu, X. L.; Yun, D. Q.; Zhang, Q.; Xie, S. Y.; Zheng, L. S. Corannulene-Based Hole-Transporting Material for Efficient and Stable Perovskite Solar Cells. *Cell Reports Phys. Sci.* **2021**, *2* (12), 100662. https://doi.org/10.1016/j.xcrp.2021.100662.

(31) Jeon, N. J.; Lee, H. G.; Kim, Y. C.; Seo, J.; Noh, J. H.; Lee, J.; Seok, S. Il. O-Methoxy

Substituents in Spiro-OMeTAD for Efficient Inorganic–Organic Hybrid Perovskite Solar Cells. *J. Am. Chem. Soc.* **2014**, *136* (22), 7837–7840. https://doi.org/10.1021/ja502824c.

(32) Hammett, L. P. The Effect of Structure upon the Reactions of Organic Compounds. Benzene Derivatives. *J. Am. Chem. Soc.* **1937**, *59* (1), 96–103. https://doi.org/10.1021/ja01280a022.

(33) Ulman, A. Formation and Structure of Self-Assembled Monolayers. *Chem. Rev.* **1996**, *96*, 1533–1554.

(34) Aktas, E.; Jiménez-López, J.; Azizi, K.; Torres, T.; Palomares, E. Self-Assembled Zn Phthalocyanine as a Robust p-Type Selective Contact in Perovskite Solar Cells. *Nanoscale Horizons* **2020**, *5* (10), 1415–1419. https://doi.org/10.1039/d0nh00443j.

(35) Brennan, B. J.; Llansola Portolés, M. J.; Liddell, P. A.; Moore, T. A.; Moore, A. L.; Gust, D. Comparison of Silatrane, Phosphonic Acid, and Carboxylic Acid Functional Groups for Attachment of Porphyrin Sensitizers to TiO2 in Photoelectrochemical Cells. *Phys. Chem. Chem. Phys.* **2013**, *15* (39), 16605–16614. https://doi.org/10.1039/c3cp52156g.

(36) Tozlu, C.; Mutlu, A.; Can, M.; Havare, A. K.; Demic, S.; Icli, S. Effect of TiO 2 Modification with Amino-Based Self-Assembled Monolayer on Inverted Organic Solar Cell. *Appl. Surf. Sci.* **2017**, *422*, 1129–1138. https://doi.org/10.1016/j.apsusc.2017.06.128.

(37) Lee, H.-L.; Flynn, N. T. X-RAY PHOTOELECTRON SPECTROSCOPY. In *Handbook of Applied Solid State Spectroscopy*; Springer US: Boston, MA; pp 485–507. https://doi.org/10.1007/0-387-37590-2_11.

(38) Yan, C.; Zharnikov, M.; Gölzhäuser, A.; Grunze, M. Preparation and Characterization of Self-Assembled Monolayers on Indium Tin Oxide. *Langmuir* **2000**, *16* (15), 6208–6215. https://doi.org/10.1021/la000128u.

(39) Saliba, M.; Matsui, T.; Seo, J.-Y.; Domanski, K.; Correa-Baena, J.-P.; Nazeeruddin, M. K.; Zakeeruddin, S. M.; Tress, W.; Abate, A.; Hagfeldt, A.; Grätzel, M. Cesium-Containing Triple Cation Perovskite Solar Cells: Improved Stability, Reproducibility and High Efficiency. *Energy Environ. Sci.* **2016**, *9* (6), 1989–1997. https://doi.org/10.1039/C5EE03874J.

(40) Costa, J. C. S.; Taveira, R. J. S.; Lima, C. F. R. A. C.; Mendes, A.; Santos, L. M. N. B. F. Optical Band Gaps of Organic Semiconductor Materials. *Opt. Mater. (Amst).* **2016**, *58*, 51–60. https://doi.org/10.1016/j.optmat.2016.03.041.

(41) Al-Ashouri, A.; Magomedov, A.; Roß, M.; Jošt, M.; Talaikis, M.; Chistiakova, G.; Bertram, T.; Márquez, J. A.; Köhnen, E.; Kasparavičius, E.; Levcenco, S.; Gil-Escrig, L.; Hages, C. J.; Schlatmann, R.; Rech, B.; Malinauskas, T.; Unold, T.; Kaufmann, C. A.; Korte, L.; Niaura, G.; Getautis, V.; Albrecht, S. Conformal Monolayer Contacts with Lossless Interfaces for Perovskite Single Junction and Monolithic Tandem Solar Cells. *Energy Environ. Sci.* **2019**, *12* (11), 3356–3369. https://doi.org/10.1039/c9ee02268f.

(42) Bharath, D.; Sasikumar, M.; Chereddy, N. R.; Vaidya, J. R.; Pola, S. Synthesis of New 2-((5-(4-Alkyl-4H-Dithieno[3,2-b:2″,3″-d]Pyrrol-2-Yl)Thiophen-2-Yl)Methylene)Malononitrile: Dopant Free Hole Transporting Materials for Perovskite Solar Cells with High Power Conversion Efficiency. *Sol. Energy* **2018**, *174* (August), 130–138. https://doi.org/10.1016/j.solener.2018.09.002.

(43) Havare, A. K.; Can, M.; Tozlu, C.; Kus, M.; Okur, S.; Demic, Ş.; Demirak, K.; Kurt, M.; Icli, S. Charge Transfer through Amino Groups-Small Molecules Interface Improving the Performance of Electroluminescent Devices. *Opt. Mater. (Amst).* **2016**, *55*, 94–101. https://doi.org/10.1016/j.optmat.2016.03.020.

(44) Bi, D.; Yi, C.; Luo, J.; Décoppet, J. D.; Zhang, F.; Zakeeruddin, S. M.; Li, X.; Hagfeldt, A.; Grätzel, M. Polymer-Templated Nucleation and Crystal Growth of Perovskite Films for Solar Cells with Efficiency Greater than 21%. *Nat. Energy* **2016**, *1* (10), 1–5. https://doi.org/10.1038/nenergy.2016.142.

(45) Ullah, A.; Park, K. H.; Nguyen, H. D.; Siddique, Y.; Shah, S. F. A.; Tran, H.; Park, S.; Lee, S. I.; Lee, K.; Han, C.; Kim, K.; Ahn, S.; Jeong, I.; Park, Y. S.; Hong, S. Novel Phenothiazine-Based Self-Assembled Monolayer as a Hole Selective Contact for Highly Efficient and Stable P-i-n Perovskite Solar Cells. *Adv. Energy Mater.* **2021**, No. November, 2103175. https://doi.org/10.1002/aenm.202103175.

(46) Hutter, E. M.; Kirchartz, T.; Ehrler, B.; Cahen, D.; von Hauff, E. Pitfalls and Prospects of Optical Spectroscopy to Characterize Perovskite-Transport Layer Interfaces. *Appl. Phys. Lett.* **2020**, *116* (10), 100501. https://doi.org/10.1063/1.5143121.

(47) Ran, J.; Yuan, P.; Xie, H. P.; Wan, F.; Chen, Y.; Yuan, Y.; He, M.; Li, J.; Wang, X.; Pan, A.; Gao, Y.; Yang, B. Triphenylamine–Polystyrene Blends for Perovskite Solar Cells with Simultaneous Energy Loss Suppression and Stability Improvement. *Sol. RRL* **2020**, *4* (12), 1–8. https://doi.org/10.1002/solr.202000490.

(48) Aktas, E.; Jiménez-López, J.; Rodríguez-Seco, C.; Pudi, R.; Ortuño, M. A.; López, N.; Palomares, E. Supramolecular Coordination of Pb 2+ Defects in Hybrid Lead Halide Perovskite Films Using Truxene Derivatives as Lewis Base Interlayers. *ChemPhysChem* **2019**, *20* (20), 2702–2711. https://doi.org/10.1002/cphc.201900068.

(49) Yang, L.; Xiao, Y.; Han, G.; Chang, Y.; Zhang, Y.; Hou, W.; Lin, J.-Y.; Li, H. Enhanced Stability and Efficiency of Perovskite Solar Cells via Bifunctional Group Passivation with Thiosalicylic Acid. *Org. Electron.* **2020**, *81*, 105681. https://doi.org/10.1016/j.orgel.2020.105681.

(50) Noel, N. K.; Abate, A.; Stranks, S. D.; Parrott, E. S.; Burlakov, V. M.; Goriely, A.; Snaith, H. J. Enhanced Photoluminescence and Solar Cell Performance via Lewis Base Passivation of Organic–Inorganic Lead Halide Perovskites. *ACS Nano* **2014**, *8* (10), 9815–9821. https://doi.org/10.1021/nn5036476.

(51) Rodríguez-Seco, C.; Méndez, M.; Roldán-Carmona, C.; Pudi, R.; Nazeeruddin, M. K.; Palomares, E. J. Minimization of Carrier Losses for Efficient Perovskite Solar Cells through Structural Modification of Triphenylamine Derivatives. *Angew. Chemie* **2020**, *132* (13), 5341–5345. https://doi.org/10.1002/ange.201915022.

(52) Roose, B.; Dey, K.; Chiang, Y.-H.; Friend, R. H.; Stranks, S. D. Critical Assessment of the Use of Excess Lead Iodide in Lead Halide Perovskite Solar Cells. *J. Phys. Chem. Lett.* **2020**, *11* (16), 6505–6512. https://doi.org/10.1021/acs.jpclett.0c01820.

(53) Chen, Y.; Meng, Q.; Xiao, Y.; Zhang, X.; Sun, J.; Han, C. B.; Gao, H.; Zhang, Y.; Lu, Y.; Yan, H. Mechanism of PbI2 in Situ Passivated Perovskite Films for Enhancing the Performance of Perovskite Solar Cells. *ACS Appl. Mater. Interfaces* **2019**, *11* (47), 44101–44108. https://doi.org/10.1021/acsami.9b13648.

(54) Muscarella, L. A.; Hutter, E. M.; Sanchez, S.; Dieleman, C. D.; Savenije, T. J.; Hagfeldt, A.; Saliba, M.; Ehrler, B. Crystal Orientation and Grain Size: Do They

Determine Optoelectronic Properties of MAPbI3 Perovskite? *J. Phys. Chem. Lett.* **2019**, *10* (20), 6010–6018. https://doi.org/10.1021/acs.jpclett.9b02757.

(55) Le Bail, A.; Jouanneaux, A. A Qualitative Account for Anisotropic Broadening in Whole-Powder-Diffraction-Pattern Fitting by Second-Rank Tensors. *J. Appl. Crystallogr.* **1997**, *30* (3), 265–271. https://doi.org/10.1107/S0021889896011922.

(56) Wang, T.; Xie, M.; Abbasi, S.; Cheng, Z.; Liu, H.; Shen, W. High Efficiency Perovskite Solar Cells with Tailorable Surface Wettability by Surfactant. *J. Power Sources* **2020**, *448* (December 2019), 227584. https://doi.org/10.1016/j.jpowsour.2019.227584.

(57) Chen, Y.; Xu, X.; Cai, N.; Qian, S.; Luo, R.; Huo, Y.; Tsang, S. Rational Design of Dopant-Free Coplanar D-π-D Hole-Transporting Materials for High-Performance Perovskite Solar Cells with Fill Factor Exceeding 80%. *Adv. Energy Mater.* **2019**, *9* (39), 1901268. https://doi.org/10.1002/aenm.201901268.

(58) Al-Dainy, G. A.; Watanabe, F.; Kannarpady, G. K.; Ghosh, A.; Berry, B.; Biris, A. S.; Bourdo, S. E. Optimizing Lignosulfonic Acid-Grafted Polyaniline as a Hole-Transport Layer for Inverted CH3NH3PbI3 Perovskite Solar Cells. *ACS Omega* **2020**, *5* (4), 1887–1901. https://doi.org/10.1021/acsomega.9b03451.

(59) Saliba, M.; Matsui, T.; Seo, J.-Y. Y.; Domanski, K.; Correa-Baena, J.-P. P.; Nazeeruddin, M. K.; Zakeeruddin, S. M.; Tress, W.; Abate, A.; Hagfeldt, A.; Grätzel, M. Cesium-Containing Triple Cation Perovskite Solar Cells: Improved Stability, Reproducibility and High Efficiency. *Energy Environ. Sci.* **2016**, *9* (6), 1989–1997. https://doi.org/10.1039/c5ee03874j.

(60) Liu, X.; Liu, Z.; Ye, H.; Tu, Y.; Sun, B.; Tan, X.; Shi, T.; Tang, Z.; Liao, G. Novel Efficient C60-Based Inverted Perovskite Solar Cells with Negligible Hysteresis. *Electrochim. Acta* **2018**, *288*, 115–125. https://doi.org/10.1016/j.electacta.2018.09.004.

(61) Chen, R.; Bu, T.; Li, J.; Li, W.; Zhou, P.; Liu, X.; Ku, Z.; Zhong, J.; Peng, Y.; Huang, F.; Cheng, Y.-B.; Fu, Z. Efficient and Stable Inverted Planar Perovskite Solar Cells Using a Triphenylamine Hole-Transporting Material. *ChemSusChem* **2018**, *11* (9), 1467–1473. https://doi.org/10.1002/cssc.201800476.

(62) Chen, C.; Zhang, S.; Wu, S.; Zhang, W.; Zhu, H.; Xiong, Z.; Zhang, Y.; Chen, W. Effect of BCP Buffer Layer on Eliminating Charge Accumulation for High Performance of Inverted Perovskite Solar Cells. *RSC Adv.* **2017**, *7* (57), 35819–35826. https://doi.org/10.1039/C7RA06365B.

(63) An, Q.; Paulus, F.; Becker-Koch, D.; Cho, C.; Sun, Q.; Weu, A.; Bitton, S.; Tessler, N.; Vaynzof, Y. Small Grains as Recombination Hot Spots in Perovskite Solar Cells. *Matter* **2021**, *4* (5), 1683–1701. https://doi.org/10.1016/j.matt.2021.02.020.

(64) Li, S.; Cao, Y. L.; Li, W. H.; Bo, Z. S. A Brief Review of Hole Transporting Materials Commonly Used in Perovskite Solar Cells. *Rare Met.* **2021**, *40* (10), 2712–2729. https://doi.org/10.1007/s12598-020-01691-z.

(65) Saliba, M.; Etgar, L. Current Density Mismatch in Perovskite Solar Cells. *ACS Energy Lett.* **2020**, *5* (9), 2886–2888. https://doi.org/10.1021/acsenergylett.0c01642.

(66) Chakravarthi, N.; Park, H.-Y.; Kranthiraja, K.; Kim, H.; Shin, J.; Song, M.; Jin, S.-H. Substituent Position Engineering of Phosphine Oxide Functionalized Triazine-Based Cathode Interfacial Materials for Flexible Organic and Perovskite Solar Cells. *Org. Electron.* **2018**, *54*, 54–63. https://doi.org/10.1016/j.orgel.2017.12.017.

(67) Correa-Baena, J.-P.; Anaya, M.; Lozano, G.; Tress, W.; Domanski, K.; Saliba, M.; Matsui, T.; Jacobsson, T. J.; Calvo, M. E.; Abate, A.; Grätzel, M.; Míguez, H.; Hagfeldt, A. Unbroken Perovskite: Interplay of Morphology, Electro-Optical Properties, and Ionic Movement. *Adv. Mater.* **2016**, *28* (25), 5031–5037. https://doi.org/10.1002/adma.201600624.

(68) Phung, N.; Al-Ashouri, A.; Meloni, S.; Mattoni, A.; Albrecht, S.; Unger, E. L.; Merdasa, A.; Abate, A. The Role of Grain Boundaries on Ionic Defect Migration in Metal Halide Perovskites. *Adv. Energy Mater.* **2020**, *10* (20), 1903735. https://doi.org/10.1002/aenm.201903735.

Table of Contents